Nanoscale

Accepted Manuscript

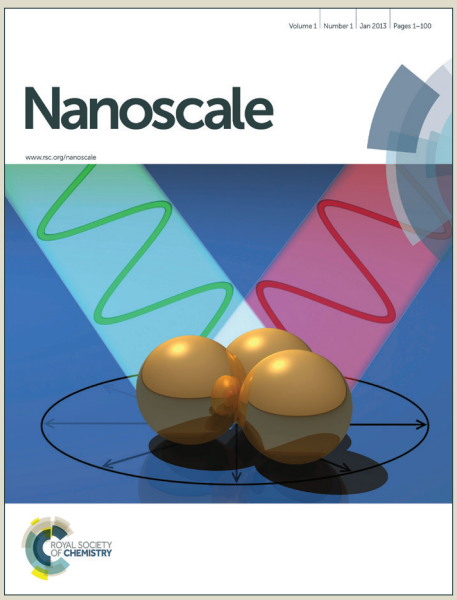

ROYAL SOCIETY OF CHEMISTRY

www.rsc.org/nanoscale

Nanoscale

RSCPublishing

ARTICLE

Facile synthesis of Rh-Pd alloy nanodendrites as highly active and durable electrocatalysts for oxygen reduction reaction

Cite this: DOI: 10.1039/x0xx00000x

Received 00th January 2012,
Accepted 00th January 2012

DOI: 10.1039/x0xx00000x

www.rsc.org/

Yue Qi,[a,§] Jianbo Wu,[b,§] Hui Zhang,*[a] Yingying Jiang,[c] Chuanhong Jin,[c] Maoshen Fu,[d] Hong Yang,[b] and Deren Yang[a]

In addition to activity, durability of Pd-based catalysts in a highly corrosive medium has become one of the most important barriers to limit their industrial applications such as low-temperature fuel cell technologies. Here, Rh with a unique capability to resist against oxidation etching was incorporated into Pd-based catalysts to enhance both of their activity and durability for oxygen reduction reaction (ORR). This idea was achieved through the synthesis of the Rh-Pd alloy nanodendrites by co-reducing Rh and Pd salt precursors in oleylamine (OAm) containing cetyltrimethylammonium bromide (CTAB). In this synthesis, Rh-Pd alloy nanostructures with Rh/Pd atomic ratios from 19:1 to 1:4 were generated by varying the molar ratios of Rh and Pd salt precursors. Interestingly, this variation on the molar ratios of the precursors from Rh rich to Pd rich would lead to the shape evolution of Rh-Pd alloy from dendritic nanostructures to spherical aggregations. We found that Br^- ions derived from CTAB were also indispensible to the production of Rh-Pd alloy nanodendrites. Owing to the addition of highly stable Rh as well as the radical structure with a large number of low-coordinated sites on the arms, Rh-Pd alloy nanodendrites with a Rh/Pd atomic ratio of 4:1 ($Rh_{80}Pd_{20}$) exhibited a substantially enhanced electrocatalytic performance towards ORR with a 5% loss of mass activity during the accelerated stability test for 10,000 cycles compared to ~50% loss of the commercial Pt/C (E-TEK).

Introduction

Over the past few decades, the ever-increasing environmental problems and up-coming depletion of fossil fuels have stimulated intense research on alternative energy conversion and storage devices as clean and sustainable energy sources.[1-3] Fuel cell operated with the electrochemical oxidation of various fuels (e.g. hydrogen, methanol, and formic acid) at the anode and the reduction of oxygen at the cathode is an attractive candidate as a promising energy-conversion device for powering portable electronic devices and vehicles due to its high-energy conversion efficiency, low pollutant emission and high-power density.[4-6] As well-known, oxygen reduction reaction (ORR) electrocatalyst is a critical and determining component of the fuel cell technology, due to its extremely slow reaction kinetics, high cost from the major component (noble metal), and corrosion-induced instability issue at cathode side.[7,8] To date, Pt-based materials are the most widely used ORR electrocatalysts at cathode in polymer electrolyte membrane fuel cells (PEMFCs) owing to their excellent catalytic activity. [9-15] However, the extremely rare abundance and prohibitive cost of Pt severely limit widespread commercialization of the PEMFC technology. To overcome these limitations, Pd-based catalysts have been recently received considerable attention as a substitute of Pt because Pd not only possesses catalytic properties similar to those of Pt, but also is relatively inexpensive and more abundant relative to Pt.[16,17] Despite tremendous efforts, developing Pd-based catalysts with high activity and long-term stability towards ORR still remains a great challenge.

Bimetallic nanocrystals consisting of two distinct metal elements in different forms (e.g., alloys, dendrites, and core-shells) provide a promising strategy to enhance catalytic performance in terms of activity and stability due to a possible synergistic effect between these two metals.[18-21] According to Nørskov, Mavrikakis, and Adzic's works,[22-24] for example, a small lattice mismatch between Pt and Pd, together with the change in the d-band center of Pt caused by its coupling with Pd, makes Pd-Pt bimetallic nanocrystals attractive catalysts with enhanced activity and stability for a variety of reactions. For a Pd-based catalyst, a rich variety of metals (M= Au, Fe, Co, Ni, Cu, and Rh) have also been exploited to produce Pd-M bimetallic nanocrystals by combining Pd with these metals for tuning and optimizing its catalytic performance.[25-28] From the viewpoint of stability, Rh is a superior candidate as an indispensible component in Pd-based catalysts because this metal has much stronger resistance against the aggressive

corrosion from the reaction medium in PEMFCs than the aforementioned others,[29,30] and thus received unremitting interest. For instance, Xia and co-workers demonstrated the synthesis of Rh-Pd bimetallic nanocubes with a core-frame structure and concave faces through a combination of kinetic control and selective capping on Pd {100} facets by Br^- ions.[31] In a recent study, Tsung and co-workers reported an iodide-mediated approach to the synthesis of Rh-Pd bimetallic core-shell nanocrystals and their attractive electrocatalytic activity toward formic acid oxidation reaction.[32] Compared to their core-shell structures, preparation of Rh-Pd alloy nanocrystals with well-defined shapes is much more complicated and difficult to be achieved by co-reduction of these two metal precursors, due to the relatively large difference in redox potential between these two metal ions (e.g., 0.915 V for Pd^{2+}/Pd and 0.8 V for Rh^{3+}/Rh versus RHE).[33]

In parallel, maneuvering the shape of noble-metal nanocrystals provide another promising strategy to enhance their catalytic properties since this parameter determines not only the facets but also the arrangements of surface atoms at corners, edges, and terraces.[34-36] Among various shapes, nanodendrites composed of highly branched arms are of particular interest for catalysis, as they had a reasonably large surface area and potentially high specific activity due to the presence of low coordinated sites (e.g., steps) with high densities on these branches.[37] In general, seeded growth has proved to be a facile and versatile approach to the synthesis of noble-metal nanodendrites by using the preformed nanocrystals with well-defined shapes as the seeds. For example, Xia and co-workers reported a seed-mediated approach for the synthesis of Pd-Pt bimetallic nanodendrites with substantially enhanced catalytic properties towards ORR relative to commercial Pt/C.[9] In another study, Han and co-workers demonstrated the synthesis of a Pt dendritic shell on structured Au cores (e.g., cubes, octahedrons, and rods) as ORR catalysts with higher activity and durability compared to the monometallic Pt catalysts.[38] Although significant progress has been made in the synthesis of bimetallic nanodendrites, few of work involves in a system consisting of Rh and Pd, particularly in the case of their alloy nanodendrites.[39]

Herein, we report a facile approach for the synthesis of Rh-Pd alloy nanodendrites with controllable compositions as well as their excellent performance as ORR catalysts. These dendritic nanostructures consisting of an aggregated core and densely straight arms were generated through an oriented attachment-based aggregation under thermodynamic control followed by a preferential overgrowth process. In addition, we found that Br^- ion played a key role in the formation of such pure phase of Rh-Pd alloy nanodendrites with dense and straight arms. The carbon supported Rh-Pd alloy nanodendrites (Rh-Pd/C) with different atomic ratios of Rh/Pd were also evaluated as catalysts for ORR. Significantly, the catalysts with a Rh/Pd molar ratio of 4:1 (i.e., $Rh_{80}Pd_{20}$/C) exhibited substantially enhanced catalytic properties in terms of activity and stability towards ORR compared to carbon supported Rh nanodendrites (Rh/C) owing to their synergetic effect between these two metals, together with the presence of low coordinated sites (e.g., high-index facets and steps) on the straight arms.

Experimental section

Synthesis of Rh-Pd Alloy Nanodendrites.

Rh-Pd alloy nanodendrites were prepared by co-reducing rhodium(II) trifluoroacetate dimer $[(CF_3COO)_2Rh]_2$ and palladium(II) acetylacetonate $[Pd(acac)_2]$ in the presence of cetyltrimethylammonium bromide (CTAB) at 200 °C, with oleylamine (OAm) as both reducing agent and solvent. In a standard procedure, 300 mg of CTAB and 5 mL of OAm were mixed in a glass vial and the mixture was pre-heated to 200 °C in air under magnetic stirring. Meanwhile, 20 mg of $[(CF_3COO)_2Rh]_2$ and 9 mg of $Pd(acac)_2$ (the Rh/Pd molar ratio was 2:1) were dissolved in 3 mL of OAm. The solution containing Rh and Pd salt precursors was then dropped into the pre-heated OAm containing CTAB. After that, the reaction mixture was maintained at 200 °C for 3 h in air. Finally, the solution was centrifuged and washed three times with ethanol and hexane to remove CTAB and OAm before characterization. In addition, we systematically investigated the effects of a number of experimental parameters, including the molar ratio of Rh/Pd salt precursors, the duration of the reaction, the amount of CTAB as well as the temperature on the final morphology of resultant Rh-Pd alloy nanodendrites.

Morphological, Structural, and Compositional Characterizations.

The obtained samples were characterized by X-ray powder diffraction (XRD) using a Rigaku D/max-ga x-ray diffractometer with graphite monochromatized Cu Kα radiation (λ = 1.54178 Å). Transmission electron microscopy (TEM) images were taken using a JEM-1200EX microscope operated at 80 kV. High-resolution transmission electron microscopy (HRTEM) was performed using a FEI Tecnai F30 G2 microscope operated at 300 kV. High-angle annular dark-field scanning TEM (HAADF-STEM) and Energy dispersive X-ray (EDX) mapping analyses were taken on a Cs-corrected STEM (TitanG2 80-200 ChemiSTEM equipped with a Super-X EDX detector system), operated at 200 kV using a probe with 50 pA beam current and a converge angle of 21.4 mrad.

Preparation of Carbon-Supported Catalysts.

The carbon supported Rh-Pd catalysts (RhPd/C) were prepared according to the previous report with some minor modifications.[10] In a standard preparation, carbon black (Vulcan XC-72) particles were dispersed in chloroform and sonicated for 30 min. A designed amount of Rh-Pd alloy nanodendrites with weight percentage of 20% were then added to this dispersion. This mixture was further sonicated for 10 min and stirred for 12 h. The resultant solids were precipitated out by centrifugation and re-dispersed in n-butylamine at a concentration of 0.5 mg-catalyst/mL. After that, the mixture was kept under stirring for 3 days, and then centrifuged and washed three times with methanol.

Electrochemical Measurement.

A three-electrode cell was used to measure the electrochemical performances of Rh-Pd/C catalysts. The working electrode was a glassy-carbon rotating disk electrode (RDE) (area: ~0.2 cm^2). A 1×1 cm^2 platinum foil and a HydroFlex hydrogen electrode were used as the counter and reference electrodes, respectively. The reference electrode was placed in a separate compartment connected with main cell via a salt bridge. Hydrogen evolution reaction (HER) was used to calibrate the reference electrode before all the tests. All potentials were referenced to the reversible hydrogen electrode (RHE). The electrolyte for cyclic voltammetry (CV)

measurement was 0.1-M $HClO_4$ solution, diluted from 70% double-distilled perchloric acid (GFS Chemicals, USA) with Millipore ultrapure water (18.2 mΩ). To prepare the working electrode, 5 mg of Rh-Pd/C or Rh/C catalysts was dispersed in 10 mL of a mixed solvent and sonicated for 10 min. The solvent contained a mixture of de-ionized water, isopropanol, and 5% Nafion 117 solution at the volumetric ratio of 8:2:0.05. 20 μL of the catalyst ink was added onto the RDE and dried in air. The loading amount of Rh-Pd alloy catalysts on the RDE was determined to be ~10 $\mu g_{metal}/cm^2$. The electrochemical active surface area (ECSA) was determined from the CV curves, calculating the amount of charges due to the desorption of hydrogen species that was obtained by integrating hydrogen desorption region after double layer correction. The CV measurement was carried in argon-saturated 0.1-M $HClO_4$ solution at room temperature with a scan rate of 50 mV/s. ORR activities were determined at the rotating rate of 1600 rpm in a 0.1-M KOH solution, which was purged with oxygen for 30 min prior to the testing. The scan rate for ORR measurement was set at 10 mV/s. Data were used without iR-drop correction. The accelerated stability test (ADT) was carried out in 0.1 M KOH between 0.6 and 1.0 V at a scan rate of 100 mV/s for 10,000 cycles.

Results and discussion

Figure 1 shows morphological, structural, and compositional characterizations of the Rh-Pd alloy nanodendrites that were obtained by the afore-mentioned approach with the molar ratio of Rh and Pd salt precursors being 2:1 in the solution (i.e., the standard procedure). The TEM micrograph in Figure 1a clearly shows that most of the Rh-Pd nanostructures had a dendritic shape, with dense and straight arms protruded from a sphere-like aggregated core. The overall size of such the nanodendrites was measured to be in the range of 35 to 60 nm in diameter, whereas, the straight arms were only 2-4 nm in width and 20-30 nm in length. These dendritic nanostructures were also clarified by HAADF-STEM technique (see Figure 1b). The typical HRTEM micrograph taken from several straight arms in Figure 1c clearly shows well-resolved, continuous fringes in the same orientation, indicating that the arm is a single crystal in nature. The fringes with lattice spacing of 1.93 and 2.22 Å can be indexed to {200} and {111} planes of face-centered cubic (*fcc*) Rh-Pd alloy, respectively. Moreover, the fringes with lattice spacing of 1.93 Å corresponding to the {200} facets are perpendicular to longitudinal orientation of the arm, suggesting that the arm grew along the <100> direction marked by an arrow. Interestingly, careful observation from the magnified HRTEM image (Figure 1d) indicates that the arms contained some high-index facets (e.g., {311}) and several types of surface defects such as adatom islands and steps, which might be of great significance to enhance the catalytic performance for a specific reaction.[40,41] The elemental distribution of Rh and Pd in the overall nanodendrites was measured by EDX mapping analysis. From the EDX mapping image (Figure 1e), it is indicated that the dendrites are made of an alloy, with Rh being slightly rich at the edges. This demonstration was further confirmed by the EDX mapping analysis taken from an individual arm (Figure 1f). We believe that the same crystal structure and small lattice mismatch between Rh and Pd (about 2%) were responsible for the formation of Rh-Pd alloy nanodendrites consisting of single-crystalline arms.

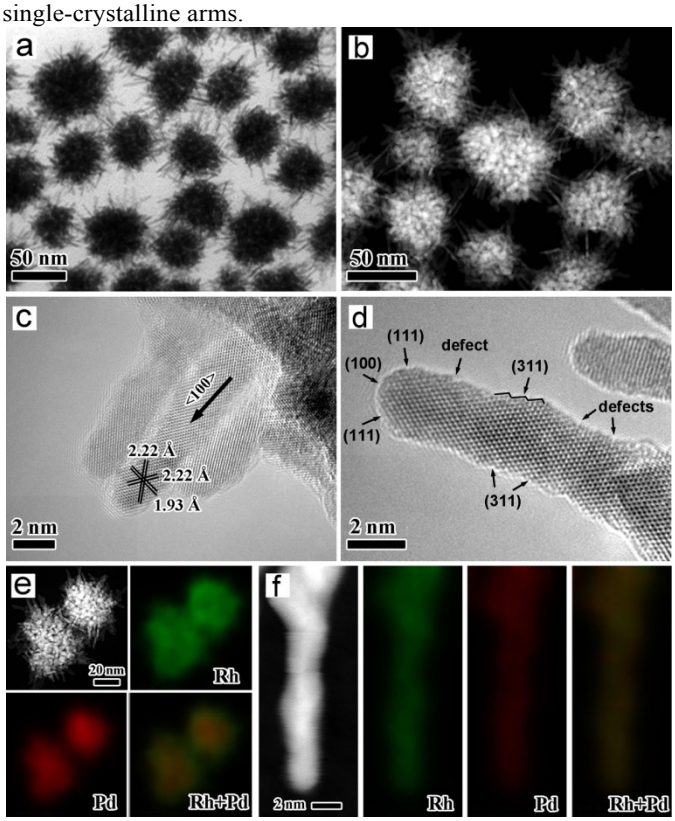

Figure 1. Characterizations of morphology, structure, and composition of the Rh-Pd alloy nanodendrites prepared using the standard procedure: (a) TEM image, (b) HAADF-STEM image, (c, d) HRTEM images, and (e, f) EDX mapping. The green and red colors in (e) and (f) correspond to Rh and Pd elements, respectively.

The composition of these Rh-Pd alloy nanostructures was readily tuned by the amounts of $[(CF_3COO)_2Rh]_2$ and $Pd(acac)_2$ supplied in the synthesis. EDX was used to characterize the composition of the Rh-Pd alloy nanostructures. On the basis of EDX analysis (see Figure S1), $Rh_{95}Pd_5$, $Rh_{80}Pd_{20}$, $Rh_{67}Pd_{33}$, $Rh_{42}Pd_{58}$, and $Rh_{20}Pd_{80}$ alloy nanostructures were obtained by varying the molar ratios of Rh and Pd salt precursors from 18:1 to 6:1, 2:1, 1:1.5, and 1:5 added in the synthesis. Figure S2 shows XRD patterns of these six samples with different compositions, including pure Rh. Obviously, all the six samples shows three well-defined diffraction peaks corresponding to (111), (200), and (220) that originated from a single *fcc* lattice in the XRD patterns. The patterns gradually shift to higher positions of 2θ with increasing the amount of Rh composition, implying the formation of alloy structure with a wide range of compositions between Rh and Pd with small lattice mismatch. According to the Vegard's Law, the molar ratios of Rh and Pd could be calculated to 88:12, 70:30, 58:42, 33:67 and 19:81, respectively, suggesting that the EDX results show a negative deviation from Vegard's Law. In addition, we found that the shape of the Rh-Pd alloy nanostructures was also varied with different molar ratios of Rh and Pd salt precursors added in the solution. Figure 2 shows typical TEM images of the Rh-Pd alloy nanostructures with different compositions, including pure Rh. From these TEM micrographs, it is clear that the Rh-

rich samples (Figure 2, a-d) preferred to form the dendritic nanostructures with dense and straight arms, whereas, the Pd-rich ones (Figure 2, e and f) were dominated by spherical aggregations consisting of numerous irregular nanoparticles. And the length and diameter of branched nanowires remained unchanged in the Rh-rich samples. We believe that this morphology variation can be attributed to the different growth behavior associated with pure Rh and Pd in this reaction condition. For Rh, the nanodendrites were mainly produced (Figure 2a). In contrast, Pd tends to form the spherical aggregations (Figure S3). The detailed mechanism will be disclosed in the following morphological evolution study with reaction time.

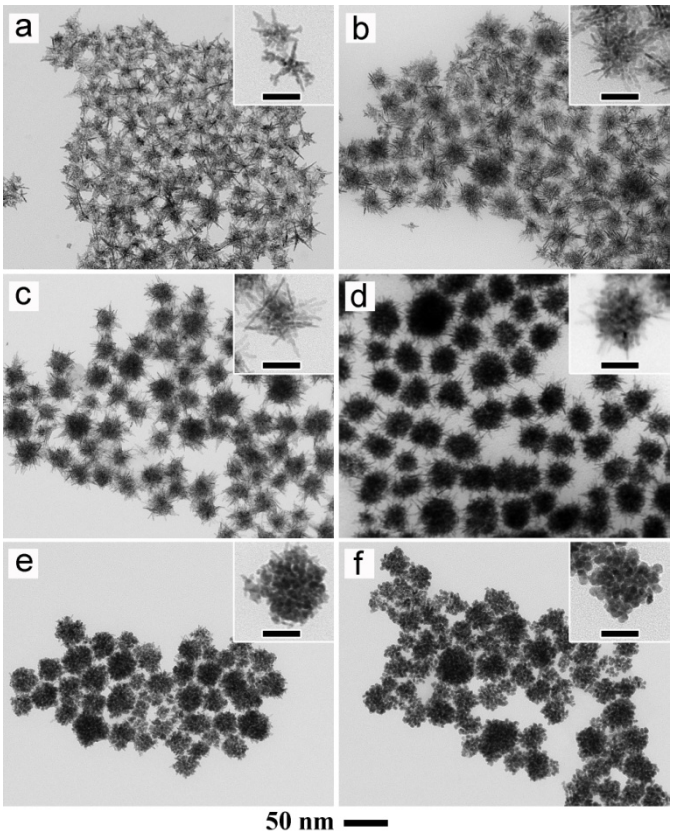

Figure 2. TEM images of Rh-Pd alloy nanostructures prepared using the standard procedure, except for the different molar ratios of Rh and Pd salt precursors added in the synthesis: (a) pure Rh, (b)18:1, (c) 6:1, (d) 2:1, (e) 1:1.5, and (f)1:5. The insets show TEM images of individual nanocrystals at a higher magnification. The scale bars in the insets are all 20 nm.

In order to clarify the formation mechanism of the Rh-Pd alloy nanodendrites, a series of samples were taken from the solution in the standard procedure by pipette at different reaction times for TEM observation, as shown in Figure 3. In the initial stage of the reaction (Figure 3a, t = 5 min), a large number of small nanoparticles with size of about 5 nm were formed. The HRTEM micrograph (inset of Figure 3a) clearly shows the oriented attachment between two adjacent nanoparticles by sharing a common crystallographic orientation along the <100> direction. As the reaction continued (Figure 3b, t = 15 min), we observed the formation of the spherical aggregations with dense cores. We believe that this morphology was caused by the extensively oriented attachment-based self-aggregation under thermodynamic control. A similar formation mechanism was also suggested for the porous and branched structures made of other noble-metals such as Pt and Au.[42] After the reaction had proceeded to t = 1.5 h, tiny tips started to grow from the surface of the spherical aggregations along the <100> direction (Figure 3c). With extension of the reaction time to 3 h, the dendritic structures with dense and straight arms were eventually generated (Figure 3d). The morphology evolution indicates that the dendritic structures were formed via two different growth habits in a sequence of oriented attachment-based self-aggregation and preferential overgrowth, which is strongly associated with the reduction rate of Rh and Pd salt precursors in the reaction. We found that Pd^{2+} ions in the form of $Pd(acac)_2$ were reduced more rapidly than Rh^{2+} ions in $[(CF_3COO)_2Rh]_2$ precursors despite the presence of Br^- ions serving as a coordinating agent to slow down the reduction rate of Pd^{2+} ions.[43] As such, the growth habit of the alloy product adopted that of pure Pd in the initial stage of the reaction and the spherical aggregations were primarily produced due to the involvement of the oriented attachment-based self-aggregation. As the reaction proceeded, the amount of Pd^{2+} ions in the solution was gradually decreased due to the rapid reduction reaction, thereby leading to the enhanced proportion of Rh^{2+} ions in the solution. After that, the growth habit of pure Rh dominated the following growth process, resulting in the formation of the nanodendrites through preferential overgrowth along the <100> direction. In addition, we believe that the diffusion between Pd and Rh during the reaction might be responsible for the formation of Rh-Pd alloy with homogeneous element distribution. This demonstration was confirmed by the addition EDX measurements on these samples that were prepared at different stages of the reaction, in which the amount of Rh was gradually increased with the reaction time (see Figure S4). This mechanism was also suggested in the synthesis of highly branched Pt-Ni alloy nanocrystals by a seed-based diffusion method.[44]

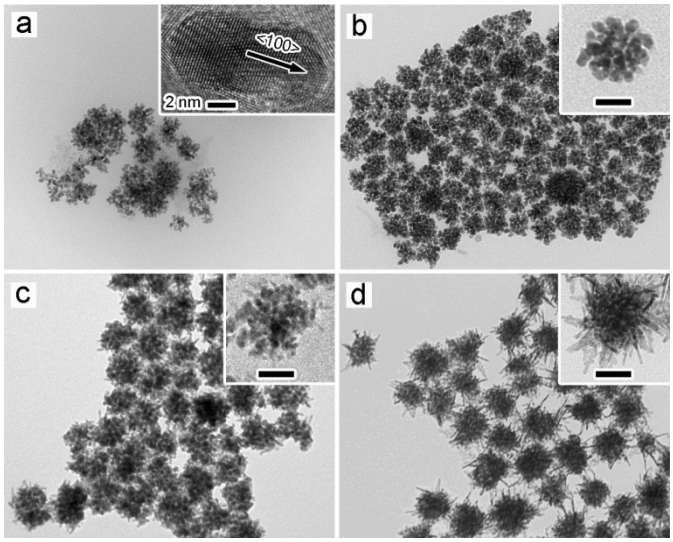

Figure 3. TEM images of the Rh-Pd alloy nanostructures prepared using the standard procedure, except for the different period of times: (a) 5 min, (b) 30 min, (c) 1 h, and (d) 3h. The inset in (a) corresponds to the HRTEM image of individual nanocrystal. The insets in (b-d) correspond to the TEM image

of individual nanocrystal at a higher magnification. The scale bars in the insets of (b-d) are all 20 nm.

We have also systematically evaluated the effects of various experimental parameters, including reaction temperatures, the amount of CTAB, and the type of capping agents, on the morphology of the resultant Rh-Pd alloy nanostructures. Figure S5 shows TEM images of the Rh-Pd nanostructures prepared using the standard procedure, except the difference in the reaction temperatures. It is clear that only the branched pods with diameters less than 5 nm were formed when the temperature was set to 140 or 160 ^{o}C (see Figure S5, a and b). An increase of the temperature to 180 ^{o}C (Figure S5c) led to the formation of the Rh-Pd alloy nanodendrites with dense and straight arms. However, the population of the dendritic nanostructures was decreased as the reaction temperature was further increased to 220 ^{o}C, as shown in Figure S5d. The optimal temperature for the synthesis of the Rh-Pd alloy nanodendrites with a production yield of about 90 % was 200 ^{o}C. These results indicate that the reaction temperature plays a key role in controlling the morphology of the Rh-Pd alloy nanostructures by manipulating the reduction rate. In addition, we found that the amount of CTAB also had a great influence on the formation of the Rh-Pd alloy nanodendrites. In the absence of CTAB (Figure S6a), two kinds of irregular nanoparticles with different sizes were generated, indicating a phase separation between Rh and Pd occurred during the synthesis due to their different redox potentials. When the amount of CTAB was less than 300 mg (e.g., 50 and 120 mg, see Figure S6, b and c), only branched Rh-Pd alloy pods were formed. As such, the amount of CTAB is also the key for the successful preparation of the Rh-Pd alloy nanodendrites because CTAB can reduce the reduction rate of Pd salt via the formation of the coordinated Pd complex (e.g., $[PdBr_4]^{2-}$).[43] The effectiveness of Br^- ions derived from CTAB can be further confirmed by replacing CTAB with the same amount of cetyltrimethylammonium chloride (CTAC, see Figure S6d). Moreover, the OAm in the preparation system, which contains amine groups, was reported to be necessary to the formation of dendritic nanostructures.[45] To clarify this demonstration, we vary the ratio of OAm in the reaction by introducing an inert oil-phase solvent, octadecylene (ODE) with different volumes. When decreasing the volume ratio of OAm and ODE (see Figure S7), the resultant Rh-Pd nanocrystals evolved from dendrites to tiny rods, indicating that OAm played a key role in the formation of the dendritic structures.

The electrocatalytic property of Rh-Pd/C catalysts was measured on the three electrode measurement. The cyclic voltammetry (CV) curves of these carbon-supported catalysts were recorded at room temperature in Ar-purged 0.1-M $HClO_4$ solutions at a sweep rate of 50 mV/s between 0.05 and 0.1 V (Figure S8). The CV curves exhibited two distinctive potential regions related to hydrogen ads/des between 0 and 0.25 V and OH ads/des at the range of 0.6~1.0 V. The electrochemically active surface area (ECSA) was calculated by measuring the charge collected in the hydrogen adsorption region assuming a value of 210μC/cm^2 for an adsorbed hydrogen monolayer on metal surface. The highly branched structure of the Rh-Pd nanodendrites provides a relatively high surface area (22 m^2/g metal for $Rh_{80}Pd_{20}$) despite their relatively large particle size, while pure Rh nanodendrite has a low ECSA (16 m^2/g metal), which is due to weak hydrogen adsorption on Rh surface.

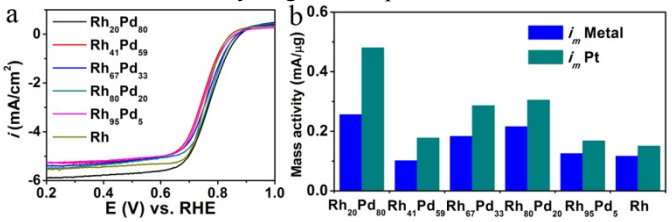

Figure 4. ORR measurement of the Rh-Pd alloy nanocrystals: (a) ORR polarization curves in 0.1-M KOH electrolyte, (b) ORR mass activities of the Rh-Pd alloy nanocrystals at 0.8 V in term of metal mass and Pt mass by equivalent cost.

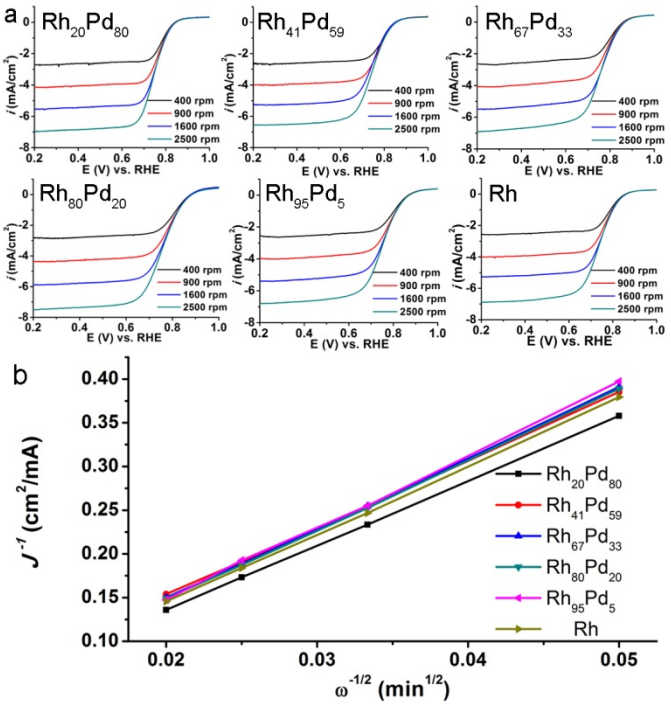

Figure 5. (a) RDE voltammograms for the ORR of six Rh-Pd/C electrocatalysts at various rotation rates. (b) Koutecky-Levich plots of the rotating disk current at 0.4 V (vs. RHE).

The electrocatalytic property of Rh-Pd dendrites in ORR was tested in 0.1-M KOH solution and compared with that of Rh dendrites catalysts (Figure 4). The ORR onset potentials were increased with the increased portion of Pd in Rh-Pd. This means oxygen reduction on Pd sites started to occur at higher potentials with a lower overpotential compared to that on Rh, indicating the Pd sites are more active than Rh. Therefore, the $Rh_{20}Pd_{80}$/C has the highest mass activity (0.26 mA/μg metal) of ORR among the five Rh-Pd/C catalysts. But the other Rh-Pd did not follow the same trend that is the Pd-rich catalyst shows a higher ORR activity. The composition dependent ORR activity shows a volcano relationship and $Rh_{80}Pd_{20}$ (0.21 mA/μg metal) is most active among the Pd-Rh/catalyst with Pd ratio below 80%. We believe that it is contributed from the highly branched structure of Pd-Rh dendrites, which has a large amount of high index sites. Those low coordinated sites could further strengthen oxygen adsorption on the Rh-Pd surface, which is much closer to the value of oxygen adsorption on Pt and enhance oxygen reduction. Considering the cost efficiency,

the loading of Rh-Pd was converted into Pt with an equivalent cost.[46] The ORR mass activity of $Rh_{20}Pd_{80}$/C was 0.48 mA/μg Pt at 0.8 V.

The electrocatalytic property of the Rh-Pd/C catalysts was examined as a function of rotation speed of the rotating disk electrode from 400 to 2500 rpm (Figure 5a).[47] The limiting current curves at various rotation speeds suggest that this region (0.2-0.6 V) is diffusion limited, indicating that the charge transfer is much faster than the mass transfer during ORR. Figure 5b shows the Koutecky–Levich plots as a function of ORR working potentials for these six Rh-Pd/C catalysts. The number of electrons transferred during the ORR was 3.70, 3.55, 3.41, 3.43, 3.28, and 3.52 for $Rh_{20}Pd_{80}$, $Rh_{41}Pd_{59}$, $Rh_{67}Pd_{33}$, $Rh_{80}Pd_{20}$, $Rh_{95}Pd_5$, and Rh, respectively.

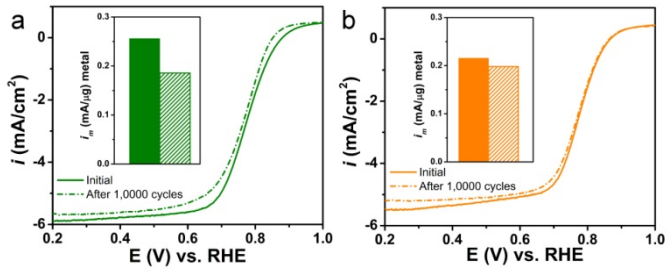

Figure 6. ORR stabilities of the $Rh_{20}Pd_{80}$ (a) and $Rh_{80}Pd_{20}$ (b) alloy nanocrystals after ADT for 10,000 cycles.

The ORR stability of the $Rh_{20}Pd_{80}$ and $Rh_{80}Pd_{20}$ catalysts was studied by accelerated stability test (ADT) for 10,000 cycles in 0.1-M KOH solution. Both the catalysts show a high stability with a half-wave potential loss of 10 mV for $Rh_{20}Pd_{80}$/C and 4 mV for $Rh_{80}Pd_{20}$/C, respectively (Figure 6). After 10,000 cycling between 0.6 and 1.0 V, the mass activity $Rh_{20}Pd_{80}$/C remains 0.19 mA/μg metal with a loss of 28% (Figure 6a) and the $Rh_{80}Pd_{20}$/C even only lost 5% in mass activity, leading to a higher activity than $Rh_{80}Pd_{20}$/C for ADT (Figure 6b). It is much more stable with the commercial Pt/C and Pd/C, which lose ~50% and 80% in the same test condition, respectively (see Figure S9). This superior stability is largely attributed to the incorporation of Rh, which has a high resistance to the base and acid etching.[28,29] It is confirmed with the stability study on pure Rh dendrites, which also showed a high stability (Figure S10).

Conclusions

In summary, we have developed a facile chemical route to the synthesis of Rh-Pd alloy nanodendrites with dense and straight arms. We found that this nanodendrite was generated through an oriented attachment-based aggregation under thermodynamic control followed by a preferential overgrowth process. The atomic ratio of Rh and Pd in this alloy could be readily tuned from 19:1 to 1:4 by varying the molar ratio of Rh and Pd salt precursors supplied in the synthesis. Interestingly, this variation on the molar ratio of the precursors from Rh rich to Pd rich also led to the shape evolution of Rh-Pd alloy from dendritic nanostructures to spherical aggregations. The Br^- ions derived from CTAB serving as a coordinating agent also played a key role in facilitating the formation of Rh-Pd alloy nanodendrites. In addition, electrochemical measurements indicated that the Rh-Pd alloy nanodendrites with a Rh/Pd atomic ratio of 4:1 (i.e., $Rh_{80}Pd_{20}$) showed the substantially enhanced specific activity towards oxygen reduction relative to others including pure Rh dendrite due to a possible synergistic effect between these two metals and the special structure on modulation of oxygen adsorption on metal surface. Significantly, this Rh-Pd alloy nanodendrite exhibited extremely higher durability than commercial Pt/C for ORR owing to the incorporation of Rh with high resistance against base and acid etching. This work not only reported a facile approach to the synthesis of bimetallic alloy nanodendrites, but also provided an effective strategy to synthesize non-Pt ORR catalysts with enhanced the ORR catalytic performance, especially durability by adding Rh metal.

Acknowledgements

This work was supported by NSFC (No. 5137222) and the Fundamental Research Funds for the Central Universities (No. 2014FZA4007). Y.J. and C.J. would like to acknowledge supports from NSFC (Grant 51222202), MOST (Grant 2014CB932500) and the Fundamental Research Funds for the Central Universities (No. 2012QNA4005).

Notes and references

[a] *State Key Laboratory of Silicon Materials, Department of Materials Science and Engineering, and Cyrus Tang Center for Sensor Materials and Applications, Zhejiang University, Hangzhou, Zhejiang 310027, P. R. China. Fax: 86-571-87952322; Tel: 86-571-87953190; E-mail: msezhanghui@zju.edu.cn*

[b] *Department of Chemical & Biomolecular Engineering, University of Illinois at Urbana-Champaign, 600 South Mathews Avenue, 114 Roger Adams Laboratory, Urbana, Illinois 61801, USA*

[c] *State Key Laboratory of Silicon Materials, Key Laboratory of Advanced Materials and Applications for Batteries of Zhejiang Province, Department of Materials Science and Engineering, Zhejiang University, Hangzhou, 310027 P. R. China*

[d] *Shaanxi Materials Analysis and Research Center, School of Materials Science and Engineering, Northwestern Polytechnical University, Xi'an, Shaanxi 710072, P. R. China*

[§] *These authors contributed equally to this work.*

† Electronic Supplementary Information (ESI) available: See DOI: 10.1039/b000000x/

1 S. Chu and A. Majumdar, *Nature*, 2012, **488**, 294-303.
2 B. Dunn, H. Kamath and J. Tarascon, *Science*, 2011, **334**, 928-935.
3 A. Arico, P. Bruce, B. Scrosati, J. Tarascon and W. Van Schalkwijk, *Nat. Mater.*, 2005, **4**, 366-377.
4 T. Wagner, B. Lakshmanan and F. Mathias, *J. Phys. Chem. Lett.* 2010, **1**, 2204-2219.
5 A. Gasteiger and M. Markovic, *Science*, 2009, **324**, 48-49.
6 M. Debe, *Nature*, 2012, **486**, 43-51.
7 H. Gasteiger, S. Kocha, B. Sompalli and F. Wagner, *Appl. Catal. B*, 2005, **56**, 9-35.
8 J. Greeley, L. Stephens, S. Bondarenko, P. Johansson, A. Hansen, F. Jaramillo, J. Rossmeisl, I. Chorkendorff and K. Nørskov, *Nature Chem.*, 2009, **1**, 552-556.
9 B. Lim, M. Jiang, P. Camargo, E. Cho, J. Tao, X. Lu, Y. Zhu and Y. Xia,

Science, 2009, **324**, 1302-1305.
10 J. Wu, J. Zhang, Z. Peng, S. Yang, T. Wagner and H. Yang, *J. Am. Chem. Soc.*, 2010, **132**, 4984-4985.
11 J. Wu, A. Gross and H. Yang, *Nano Lett.*, 2011, **11**, 798-802.
12 P. Strasser, S. Koh, T. Anniyev, J. Greeley, K. More, C. Yu, Z. Liu, S. Kaya, D. Nordlund, H. Ogasawara, F. Toney and A. Nilsson, *Nature Chem.*, 2010, **2**, 454-460.
13 Z. Chen, M. Waje, W. Li and Y. Yan, *Angew. Chem. Int. Ed.* 2007, **46**, 4060-4063.
14 J. Wang, H. Inada, L. Wu, Y. Zhu, Y. Choi, P. Liu, W. Zhou and R. Adzic, *J. Am. Chem. Soc.*, 2009, **131**, 17298-17302.
15 R. Stamenkovic, B. Fowler, S. Mun, G. Wang, N. Ross, A. Lucas, and Markovic, M. *Science*, 2007, **315**, 493-497.
16 C. Bianchini and P. Shen, *Chem. Rev.* 2009, **109**, 4183-4206.
17 E. Antolini, *Energy Environ. Sci.*, 2009, **2**, 915-931.
18 D. Wang and Y. Li, *Adv. Mater.*, 2011, **23**, 1044-1060.
19 J. Wu, P. Li, Y. Pan, S. Warren, X. Yin and H. Yang, *Chem. Soc. Rev.* 2012, **41**, 8066-8074.
20 J. Gu, Y. Zhang and F. Tao, *Chem. Soc. Rev.* 2012, **41**, 8050-8065.
21 J. Zhang, K. Sasaki, E. Sutter and R. Adzic, *Science*, 2007, **315**, 220-222.
22 J. Nørskov, T. Bligaard, J. Rossmeis and C. Christensen, *Nat. Chem.*, 2009, **1**, 37-46.
23 J. Zhang, M. Vukmirovic, Y. Xu, M. Mavrikakis and R. Adzic, *Angew. Chem. Int. Edit.*, 2005, **44**, 2132-2135.
24 K. Sasaki, H. Naohara, Y. Cai, Y. Choi, P. Liu, M. Vukmirovic, J. Wang and R. Adzic, *Angew. Chem., Int. Ed.*, 2010, **49**, 8602-8607.
25 D. Kim, Y. Lee, S. Lee and S. Han, *Angew. Chem., Int. Ed.*, 2012, **51**, 159-163.
26 V. Mazumder, M. Chi, M. Mankin, Y. Liu, O. Metin, D. Sun, K. More and S. Sun, *Nano Lett.*, 2012, **12**, 1102-1106.
27 M. Shao, *J. Power Sources*, **2011**, *196*, 2433-2444.
28 F. Tao, M. Grass, Y. Zhang, D. Butcher, J. Renzas, Z. Liu, J. Chung, B. Mun, M. Salmeron and G. Somorjai, *Science*, 2008, **322**, 932-934.
29 D. Rice and J. Suits, *J. Appl. Phys.*, 1979, **50**, 5899-5901.
30 J. Handley, *Platinum Metals Rev.*, 1989, **33**, 64-72.
31 S. Xie, N. Lu, Z. Xie, J. Wang, M. Kim and Y. Xia, *Angew. Chem., Int. Ed.*, 2012, **51**, 10266-10270.
32 B. Sneed, C. Kuo, C. Brodsky and C. Tsung, *J. Am. Chem. Soc.* 2012, **134**, 18417-18426.
33 C. Zoski, Handbook of Electrochemistry, Elsevier, Oxford, 2006, **18**, p817.
34 Y. Xia, Y. Xiong, B. Lim and S. Skrabalak, *Angew. Chem., Int. Ed.*, 2009, **48**, 60-103.
35 Z. Quan, Y. Wang and J. Fang, *Acc. Chem. Res.*, 2013, **46**, 191-202.
36 J. Wu, L. Qi, H. You, A. Gross, J. Li and H. Yang, *J. Am. Chem. Soc.*, 2012, **134**, 11880-11883.
37 B. Lim and Y. Xia, *Angew. Chem., Int. Ed.*, 2011, **50**, 76-85.
38 Y. Kim, J. Hong, Y. Lee, M. Kim, D. Kim, W. Yun and S. Han, *Angew. Chem. Int. Ed.*, 2010, **49**, 10197-10201.
39 H. Kobayashia, B. Lim, J. Wang, P. Camargo, T. Yu, M. Kim and Y. Xia, *Chem. Phys. Lett.*, 2010, **494**, 249-254.
40 N. Tian, Z. Zhou, S. Sun, Y. Ding and Z. Wang, *Science*, 2007, **316**, 732-735.
41 H. Zhang, M. Jin and Y. Xia, *Angew. Chem. Int. Ed.*, 2012, **51**, 7656-7673.
42 A. Mohanty, N. Garg and R. Jin, *Angew. Chem. Int. Ed.*, 2010, **49**, 4962-4966.
43 M. Jin, H. Zhang, Z. Xie and Y. Xia, *Angew. Chem. Int. Ed.*, 2011, **50**, 7850-7854.
44 Z. Niu, D. Wang, R. Yu, Q. Peng and Y. Li, *Chem. Sci.*, 2012, **3**, 1925-1929.
45 S. Mourdikoudis and L. M. Liz-Marzán, *Chem. Mater.*, 2013, **25**, 1465-1476.
46 The prices of Pd, Pt, Rh are based on Engelhard Industrial Bullion prices on August 8th, 2013.
47 J. B. Wu, H. Yang, *Nano Res.* 2011, **4**, 72-82.